ADVANCED MATERIALS
www.advmat.de

Visualizing Tailored Spin Phenomena in a Reduced-Dimensional Topological Superlattice

Rui Sun, Shijia Yang, Xu Yang, A. Kumar, Eric Vetter, Wenhua Xue, Yan Li, Na Li, Yang Li, Shihao Zhang, Binghui Ge, Xiang-qun Zhang, Wei He, Alexander F. Kemper, Dali Sun, and Zhao-hua Cheng**

Emergent topological insulators (TIs) and their design are in high demand for manipulating and transmitting spin information toward ultralow-power-consumption spintronic applications. Here, distinct topological states with tailored spin properties can be achieved in a single reduced-dimensional TI-superlattice, (Bi_2/Bi_2Se_3)-$(Bi_2/Bi_2Se_3)_N$ or $(\square/Bi_2Se_3)$-$(Bi_2/Bi_2Se_3)_N$ (N is the repeating unit, $\square$ represents an empty layer) by controlling the termination via molecular beam epitaxy. The Bi_2-terminated superlattice exhibits a single Dirac cone with a spin momentum splitting ≈0.5 Å^{-1}, producing a pronounced inverse Edelstein effect with a coherence length up to 1.26 nm. In contrast, the Bi_2Se_3-terminated superlattice is identified as a dual TI protected by coexisting time reversal and mirror symmetries, showing an unexpectedly long spin lifetime up to 1 ns. The work elucidates the key role of dimensionality and dual topological phases in selecting desired spin properties, suggesting a promise route for engineering topological superlattices for high-performance TI-spintronic devices.

Present spintronics seeks efficient spin current to charge current transducers in a strong spin–orbit coupling (SOC) material with a large electric conductivity for ultralow-power-consumption spintronic applications. Such strong SOC materials usually are divided into two categories, heavy metals and quantum materials, for which the spin–charge interconversion is respectively attributed to the spin Hall effect (SHE) and the Rashba–Edelstein effect (REE),[1,2] or vice versa. Emergent topological quantum materials, including topological insulators (TIs),[3–6] Dirac semimetals,[7] and Weyl metals[8–11]—as the key core of quantum material families—have been compelling due to their order of magnitudes larger charge-to-spin conversion efficiencies compared to those in heavy metals.[12,13]

While the spin-to-charge (SCC) efficiencies of most 3D TIs with a single surface state remain moderate,[14,15] the convergence of multiple nontrivial topological phases in one material, such as dual topological insulators, may suggest a new route for designing TI-based quantum materials.[16] Protected by both mirror symmetry and time reversal invariant symmetry, dual TIs would exhibit a high SCC efficiency benefiting from synergistic contributions of the coexisting TI phases. One prototypical example is $(Bi_2$-$Bi_2Se_3)_N$ topological superlattices (N is the repeating unit number), categorized as one of an infinitely adaptive TI family series consisting of alternating one bismuth bilayer (Bi BL) and one quintuple bismuth selenide layer (Bi_2Se_3 QL).[17] In

Dr. R. Sun, X. Yang, W. Xue, Dr. Y. Li, Dr. N. Li, Y. Li, Dr. S. Zhang, Dr. X.-q. Zhang, Prof. W. He, Prof. Z.-h. Cheng
Beijing National Laboratory for Condensed Matter Physics
Institute of Physics
Chinese Academy of Sciences
Beijing 100190, China
E-mail: zhcheng@iphy.ac.cn

S. Yang, Dr. A. Kumar, E. Vetter, Prof. A. F. Kemper, Prof. D. Sun
Department of Physics
North Carolina State University
Raleigh, NC 27695, USA
E-mail: dsun4@ncsu.edu

Prof. B. Ge
Key Laboratory of Structure and Functional Regulation of Hybrid Materials of Ministry of Education
Institutes of Physical Science and Information Technology
Anhui University
Hefei 230601, China

The ORCID identification number(s) for the author(s) of this article can be found under https://doi.org/10.1002/adma.202005315.

Dr. R. Sun, X. Yang, Dr. Y. Li, Dr. N. Li, Y. Li, Prof. Z.-h. Cheng
School of Physical Sciences
University of Chinese Academy of Sciences
Beijing 100049, China

E. Vetter
Department of Materials Science and Engineering
North Carolina State University
Raleigh, NC 27695, USA

Prof. D. Sun
Organic and Carbon Electronics Lab (ORaCEL)
North Carolina State University
Raleigh, NC 27695, USA

Prof. Z.-h. Cheng
Songshan Lake Materials Laboratory
Dongguan 523808, China

DOI: 10.1002/adma.202005315

the presence of strong covalent bond couplings between the Bi_2Se_3 and Bi_2 block, their coexisting nontrivial TI band structures can be tailored by varying the stacking order, termination, and thickness of the superlattices, and so forth. The electronic structure tunability in this material class may also result in rich and tunable spin properties: While the bulk Bi_2Se_3 block is a prototypical 3D TI, an isolated Bi_2 bilayer is theoretically predicted to be an elemental 2D TI,[18] and thus combining these two 2D/3D-TI building blocks at a low-dimensional limit will offer a unique opportunity for studying the role of dimensionality and dual topological phases in the pursuit of large SCC efficiencies.

Here, we report tailored spin phenomena in reduced-dimensional ($\square/Bi_2Se_3$)-$(Bi_2/Bi_2Se_3)_N$ or (Bi_2/Bi_2Se_3)-$(Bi_2/Bi_2Se_3)_N$ (N = 1, 3, 5, or 7 is the repeating unit, $\square$ represents an empty layer) TI-superlattice (referred to as Bi_2Se_3-TSL or Bi_2-TSL if not illustrated) ultrathin films by controlling the surface termination and stacking thickness via molecular beam epitaxy (MBE). Electronic structures of the prepared superlattices are characterized by angle-resolved photoemission spectroscopy (ARPES) and ab initio density functional theory (DFT) calculation, showing coexisting dual TI and topological crystalline insulator (TCI) phases for Bi_2Se_3-TSL(Bi_2Se_3-termination) and a pronounced Rashba-like Dirac surface state accompanied by a giant spin momentum splitting for the Bi_2-TSL(Bi_2-termination). By performing spin-pumping measurements, we find a maximum SCC efficiency, λ_{IEE} up to 1.26 nm for the Bi_2-TSL and 0.19 nm for Bi_2Se_3-TSL, which is roughly several times to one order of magnitude larger than that for the pristine 3D TIs (λ_{IEE} ≈ 0.035–0.075 nm).[14,15] The SCC efficiency of Bi_2-TSL sharply decays with increasing stacking thickness by relaxing the reduced dimensionality of the superlattice. Bi_2Se_3-TSL, on the other hand, exhibits a remarkably long spin lifetime up to τ_s ≈1 ns as determined by oblique Hanle precession measurements. By assessing both momentum relaxation time (τ_p) and spin lifetime (τ_s) for two terminations independently, such distinct spin properties could be attributed to the termination dependent Dyakonov–Perel scattering mechanism and the same SOC field is derived stemming from the same bulk elements. Our results not only demonstrate the essential role of superlattice band engineering in realizing multi-functional topological phase transitions but also provide a direct experimental proof of the compatibility of the low-dimensional topological superlattices for alternative, efficient spin-to-charge interconverts and long-range spin transport via stacking sequence engineering.

Figure 1a shows a schematic view of the crystal structure of Bi_2Se_3-TSL and Bi_2-TSL samples, respectively. The infinitely adaptive series of $(Bi_2/Bi_2Se_3)_N$ ($N \to \infty$) has a hexagonal layered structure with space group $R\bar{3}m$.[19] Along the c axis, the $(Bi_2/Bi_2Se_3)_N$ compound is a 1:1 natural superlattice of alternating Bi_2 and Bi_2Se_3 blocks, in which one Bi bilayer is intercalated between two van der Waals Bi_2Se_3 quintuple layers. A small lattice mismatch between these two blocks (<5%) allows the free-standing Bi_2 bilayer to reside on the surface of the Bi_2Se_3 QL layer, forming a naturally ordered stacking sequence having alternating Bi_2- or Bi_2Se_3-surface termination. It has been reported that it is challenging to mechanically cleave the interface between the Bi_2 and Bi_2Se_3 blocks in the bulk material to produce a well-defined termination without interdiffusions.[20] Here the reduced-dimensional TSLs, with alternative Bi_2 or Bi_2Se_3 termination, is realized by the MBE method (see Experimental Section). The composition and the vertical stacking order of the superlattice is validated by the cross-sectional scanning transmission electron microscopy (STEM) as shown in Figure 1b (left). The STEM image shows that the prepared Bi_2-$TSL_{N=7}$ has a crystalline structure grown along the [0001] direction where the atomic layers of Bi and Se are continuous and well-aligned at the atomic level in the absence of displacement of Bi and Se atoms. The alternative epitaxially grown Bi_2Se_3 and Bi_2 blocks are outlined by the light-blue dashed arrow, suggesting a high-quality superlattice structure. The high-quality single crystallinity of prepared films was further confirmed with X-ray diffraction (XRD) as shown in Figure 1b (right), sharing similar featured peaks with those found in bulk Bi_2Se_3 materials.

We have performed ARPES measurements to study the electronic structure of TSL for both terminations. Figure 1c,d present the measured ARPES spectra for the Bi_2Se_3-$TSL_{N=1}$ (left) and Bi_2-$TSL_{N=1}$ (right) around the Fermi level, showing the major differences between the two terminations. For the Bi_2Se_3-terminated structure, the ARPES results reveal the presence of electron-like bands above −0.8 eV, together with a clear hexagonal-warped Fermi surface shown at the center of the surface Brillouin zone, which is quite similar to 3D-TI Bi_2Se_3. The energy dispersion maps along $\overline{K}$–$\overline{\Gamma}$–$\overline{M}$ in Figure 1d (left) shows that there are quite linear, Dirac-like surface sub-bands touching each other at the $\overline{\Gamma}$ point around −0.75 eV, which is termed as a topological surface state (TSS) from TI protected by time reversal symmetry.[17,21] Remarkably, there is another hole-like band developed crossing the Dirac-like band at E_B = −0.2 eV, which indicates the coexistence of the D_{TCI} and D_{TSS} surface state, described as one of dual TIs.[22] The Fermi velocity v_F of "V"-type upturn bands is estimated to be about 5×10^5 m s^{-1}, (see Figure S2d, Supporting Information) which is comparable to the value in the pristine Bi_2Se_3 from our previous report.[23] In contrast to the warped hexagon in the Bi_2Se_3-terminated superlattice, the Fermi surface in the Bi_2-terminated sample manifests as a hexagonal snowflake with six-fold symmetry, which also demonstrates the perfect hetero-epitaxy between the alternating Bi_2Se_3 and Bi_2 layers. The energy dispersion along the $\overline{K}$–$\overline{\Gamma}$–$\overline{M}$ direction shown in the right panel of Figure 1d presents hole-like maximal momentum splitting at the Fermi level with Δk_F ≈ 0.5 Å^{-1} (see Figure S5a, Supporting Information). To the best of our knowledge, this is by far the largest spin momentum splitting ever reported.[24]

The obtained ARPES results are further corroborated by DFT calculations. Figure 1e (left) shows the considered bulk and (0001)-projected surface BZs of the primitive unit cell. Consistent with the ARPES results, the top stacking sequence can totally reshape the non-trivial surface states as demonstrated by the calculated electronic structure shown in Figure 1f,g, respectively. Whereas the TSS (D_{TSS} in Figure 1g) persists in the presence of the Bi bilayer,[20] the Bi_2Se_3 termination (Figure 1f) exhibits an electron-like band at the $\overline{\Gamma}$ point, and an odd crossing number of the electron states along surface projections $\overline{\Gamma}$–$\overline{M}$, which was classified as a non-trivial Z_2 topological invariant together with its band inversion at the $\overline{\Gamma}$ point. The calculated Dirac point was located at about

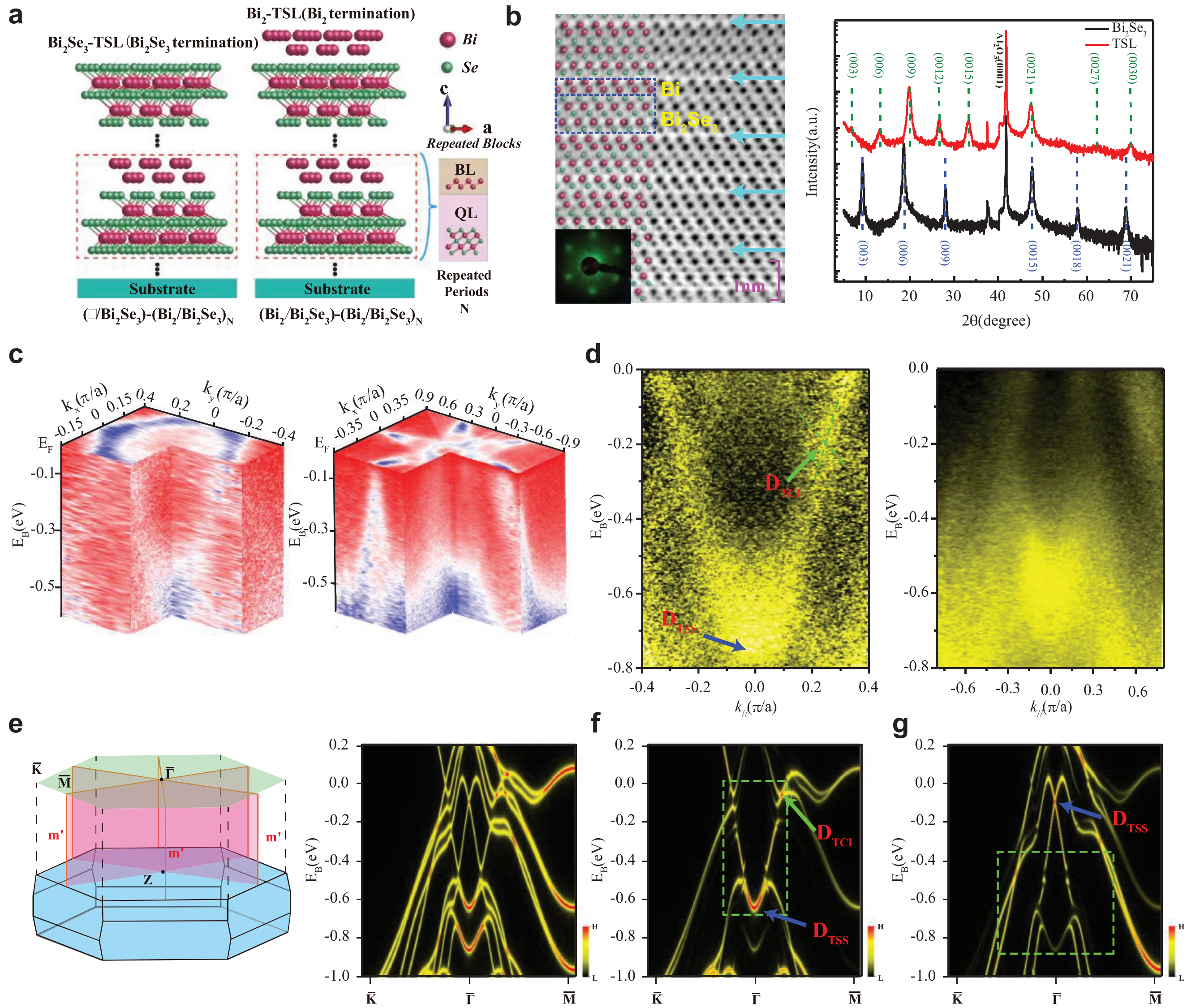

Figure 1. Structure characterizations of the topological superlattices, ($\square$/Bi_2Se_3)-(Bi_2/Bi_2Se_3)$_N$ or (Bi_2/Bi_2Se_3)-(Bi_2/Bi_2Se_3)$_N$ and the termination-dependent TSSs. a) Schematic crystal structures of the (Bi_2/Bi_2Se_3)$_N$ superlattice known as the infinitely adaptive Bi_2-Bi_2Se_3 natural superlattice phase series. The side view of TI-superlattice ($\square$/Bi_2Se_3)-(Bi_2/Bi_2Se_3)$_N$ or (Bi_2/Bi_2Se_3)-(Bi_2/Bi_2Se_3)$_N$ illustrates the alternating quintuple layer-bilayer structure (stacking period, N) with different termination: Bi_2Se_3 termination (left); Bi_2 termination (right). b) Obtained high-resolution annular bright-field STEM image and the XRD pattern of the reduced-dimensional TSL thin film grown on Si(111) substrate and Al_2O_3(0001) using MBE method, respectively. The inset on the STEM image shows in situ low-energy electron diffraction (LEED) patterns. The XRD pattern is compared to the values for the bulk Bi_2Se_3 film. c,d) Raw 3D ARPES spectra map and 2D E–k dispersion along $\bar{K}$–$\bar{\Gamma}$–$\bar{M}$ for the Bi_2Se_3 termination (left) and the Bi_2 termination (right), respectively. The measured electron structure energy dispersion $E(k_x,k_y)$ is from −0.8 to 0 eV. e) Bulk Brillouin zone and its 2D projection to (0001) surface (left) and DFT calculations of the whole band structure of the Bi_2Se_3-Bi_2-Bi_2Se_3-Bi_2 slab (right). The surface energy dispersion is along the high-symmetry line $\bar{K}$–$\bar{\Gamma}$–$\bar{M}$. The termination dependent surface states extracted from the DFT calculations are shown in (f) and (g), respectively. The crossing points denotes the coexisting D_{TCI} and D_{TSS} states along the $\bar{\Gamma}$–$\bar{M}$ (D_{TCI} point by intersected green dash lines and indicated by the green arrow in (d)) and at the $\bar{\Gamma}$ point for the Bi_2Se_3 termination, whereas only the D_{TSS} state is observed for the Bi_2 termination. The dotted green square approximately outlines the measured energy scale shown in (f) and (g) for the two terminations.

−0.7 eV which is consistent with obtained value from ARPES results. The TCI phase is derived from the existence of three Γ–Z–M mirror planes guaranteeing the avoided band crossing points along the $\bar{\Gamma}$–$\bar{M}$ projection lines. The predicted crossing points were at ≈ 0.25 Å^{-1}—a non-TRIM (time-reversal invariant momenta) along the $\bar{\Gamma}$–$\bar{M}$ direction agreeing with ARPES observation well. It is noteworthy that in spite of the predicted hybridization gap along $\bar{\Gamma}$–$\bar{K}$ lines in the calculation, there is no clear gap along same direction possibly due to the energy resolution limits (also see Figures S2a and S4a, Supporting Information).

Given that an isolated Bi_2 bilayer is predicted to be a 2D TI and bulk Bi_2Se_3 naturally possesses 3D topological properties, combining these two building blocks into the reduced-dimensional superlattice may offer a unique route for studying the effects of interlayer interactions and their effects on spin properties. Particularly, an efficient spin-to-charge conversion would be expected due to the presence of coexisting lowly dispersive surface bands in which the perpendicular locking of an electron's spin with its momentum will be strongly influenced by the reduced dimensionality and quantum confinement of the superlattice.[25] Below we characterized the SCC efficiency in NiFe/TSL heterostructures by using ferromagnetic resonance (FMR) and spin-pumping methods.

The heterostructures are prepared via in-situ MBE growth to avoid surface states contamination (see Experimental Section). The representative schematic structure of the spin-pumping experiment setup is depicted in **Figure 2**a. Figure 2b shows the magnetic field (H) dependence of the spin-pumping-induced voltage V_{SP} obtained from the NiFe/Bi_2-$TSL_{N=1}$ sample taken at microwave frequencies of 6, 9, and 14 GHz, respectively. The inset of Figure 2b shows the obtained FMR resonance field $\mu_0 H_{res}$ at different frequencies ranging from 2 to 16 GHz. Magnetic field dependence of $V_{SP}(H)$ in the NiFe/Bi_2-$TSL_{N=3}$ sample at different microwave powers are presented in Figure 2c. The inset shows that the derived V_{IEE} value is proportional to the applied microwave power, consistent with the expected spin-pumping mode.

Figure 2d compared the measured $V_{SP}(H)$ spectra in the NiFe/TSL heterostructures at four different stacking periods. Remarkably, the Bi_2-terminated samples exhibit a much larger V_{SP} compared to that from the Bi_2Se_3-terminated samples. The V_{SP} of the Bi_2-terminated samples shows a decrease while increasing the stacking period from $N = 1$ to 7 in contrast to the slightly increased response in the Bi_2Se_3-terminated samples. The extracted non-monotonic damping factor α_{eff} is plotted in Figure 2e revealing the topological origin of spin pumping. The derived spin-to-charge conversion efficiency defined as IEE length $\lambda_{IEE} = j_C^{2D}/j_S^{3D}$ (see Supporting Information) as a function of stacking period is summarized in Figure 2f. A large λ_{IEE} up to 1.26 nm is observed in the Bi_2-terminated sample with stacking period $N = 1$, whereas the IEE lengths of the Bi_2Se_3-terminated sample fluctuates between with a minimal value of 0.19 nm ($N = 1$) to 0.24 nm ($N = 5$). It is noteworthy that all of the obtained values are still 5–7 times larger than that of pristine 3D-TI Bi_2Se_3 (≈0.035 nm),[14] indicating the synergistic SCC efficiency from dual TSSs. Compared with the best reported Bi-based quantum materials as summarized in Figure 2g: λ_{IEE} = 0.05 nm in the isolated Bi layer,[26] 0.28 nm in Bi/Bi_2Se_3,[23] and 0.3 nm in the sputtered Bi_2Se_3 materials,[27] the obtained large spin-to-charge conversion in the TSLs indicates the key role of the reduced dimensionality and coexisting TSSs, as revealed in the ARPES results, in determining the spin-to-charge conversion.

In a simple approximation, the IEE length, λ_{IEE} can be expressed as $\lambda_{IEE} = v_F \cdot \tau_p$,[5,28] where τ_p is the momentum relaxation time on the TI surface state. Using the IEE lengths derived from the spin-pumping measurements and the v_F estimated from the ARPES results (see Figures S1 and S2, Supporting Information), we find the momentum relaxation time, τ_p is ≈ 2.95 fs for the Bi_2-terminated and ≈0.39 fs for the Bi_2Se_3-terminated sample ($N = 1$), respectively. Theoretically, the TSS is characterized by quite long momentum relaxation in the picosecond range as a result of forbidden backscattering events.[29] The estimated τ_p is probably modified by the transmission time across the interface or a faster spin-flip relaxation mechanism, resulting in a shorter τ_p than the original momentum scattering time in the TI.[5,30] For the spin transport phenomena in a Dirac material where spin and momentum are perpendicularly locked to each other, τ_p and spin lifetime τ_s are strongly tied to each other, for instance, $\tau_{s,EY}$ is proportional to $\tau_{p,EY}$ under the Elliot–Yafet (E–Y) scattering mechanism while $\tau_{s,\,DP}$ is inversely proportional to the $\tau_{p,DP}$ if the Dyakonov–Perel (D–P) scattering mechanism dominates.[31,32] In order to identify the dominant spin scattering mechanism for the two terminations, the characterization of τ_s in the TSL is essential.

The oblique Hanle precession measurement is taken to characterize the τ_s for two terminations, which has been successfully employed in inorganic semiconductors,[33] conjugated polymers,[34] hybrid organic-inorganic perovskites,[35] and 2DEGs,[36] and so forth. As shown in **Figure 3**a, it illustrates the precession of the spin polarization S of the injected spin current under the oblique magnetic field H with a Larmor precession frequency, $\omega_L = \hbar/g_L\mu_B(\mu_0 H)$ and the angular dependence (θ between axis x and magnetic field) of the IEE voltage signal is investigated when tilting the applied magnetic field out-of-plane from 0 to π in the (xz) plane. This Hanle spin precession modulates the spin accumulation when τ_s is comparable to the Larmor precession time $1/\omega_L$, resulting in θ-dependent IEE voltage from which τ_s can be extrapolated.[33] Based on the Landau–Lifshitz–Gilbert (LLG) equation (see Supporting Information), the resonance field $H_{res}(\theta)$ is fitted (Figure 3b), from which the magnetization angle ϕ_M is calculated as shown in Figure 3c.

Figure 3d displays the angular dependence of $V_{IEE}(\theta)/V_{IEE}(\theta = 0)$ in NiFe/Bi_2Se_3 (3QL), NiFe/Bi_2Se_3 (10QL), NiFe/Bi_2-$TSL_{N=1}$ and NiFe/Bi_2Se_3-$TSL_{N=1}$, respectively. The calculated θ dependence of V_{IEE} with three different τ_s are also presented in each panel. Whereas a sharp decrease of $V_{IEE}(\theta)$ in the pristine Bi_2Se_3 (3QL) at the high titled field angle indicates a very short spin lifetime ≈20 ps, the relatively longer τ_s in Bi_2Se_3 (10 QL) is found to be ≈150 ps. This is probably due to the formation of TSS when the top and bottom surface are decoupled above 6 QL thickness. For the TSL with two terminations, we find that the Bi_2Se_3-terminated sample exhibits a longer spin lifetime up to 1 ns compared to that of the Bi_2-terminated one (≈400 ps). The obtained nanosecond spin lifetime here is orders of magnitude longer than that in traditional heavy metals such as Pt (≈13 ps) and comparable to that of widely investigated graphene 7.8 ns with a much weaker SOC.[37,38] While the Bi_2-terminated superlattice functions as an ideal spin-to-charge converter possessing a large IEE length, the Bi_2Se_3-terminated superlattice may be more favorable for long-range spin transport. These results reinforce the key role of the reduced dimensionality and termination-dependent coexisting TSSs in tailoring the spin properties of Bi-based TI materials.

Our results demonstrate that tailored spin properties have been achieved by altering the stacking sequence of TI superlattices for different resurface terminations: The Bi_2-terminated superlattice possesses a large momentum splitting with a highly efficient SCC; we find a record high of λ_{IEE} = 1.26 nm, accompanied by τ_p = 2.95 fs and τ_s ≈ 400 ps. As for the Bi_2Se_3-terminated superlattice, whereas it exhibits a relatively lower SCC λ_{IEE} = 0.19 nm and τ_p ≈ 0.385 fs, a much longer spin

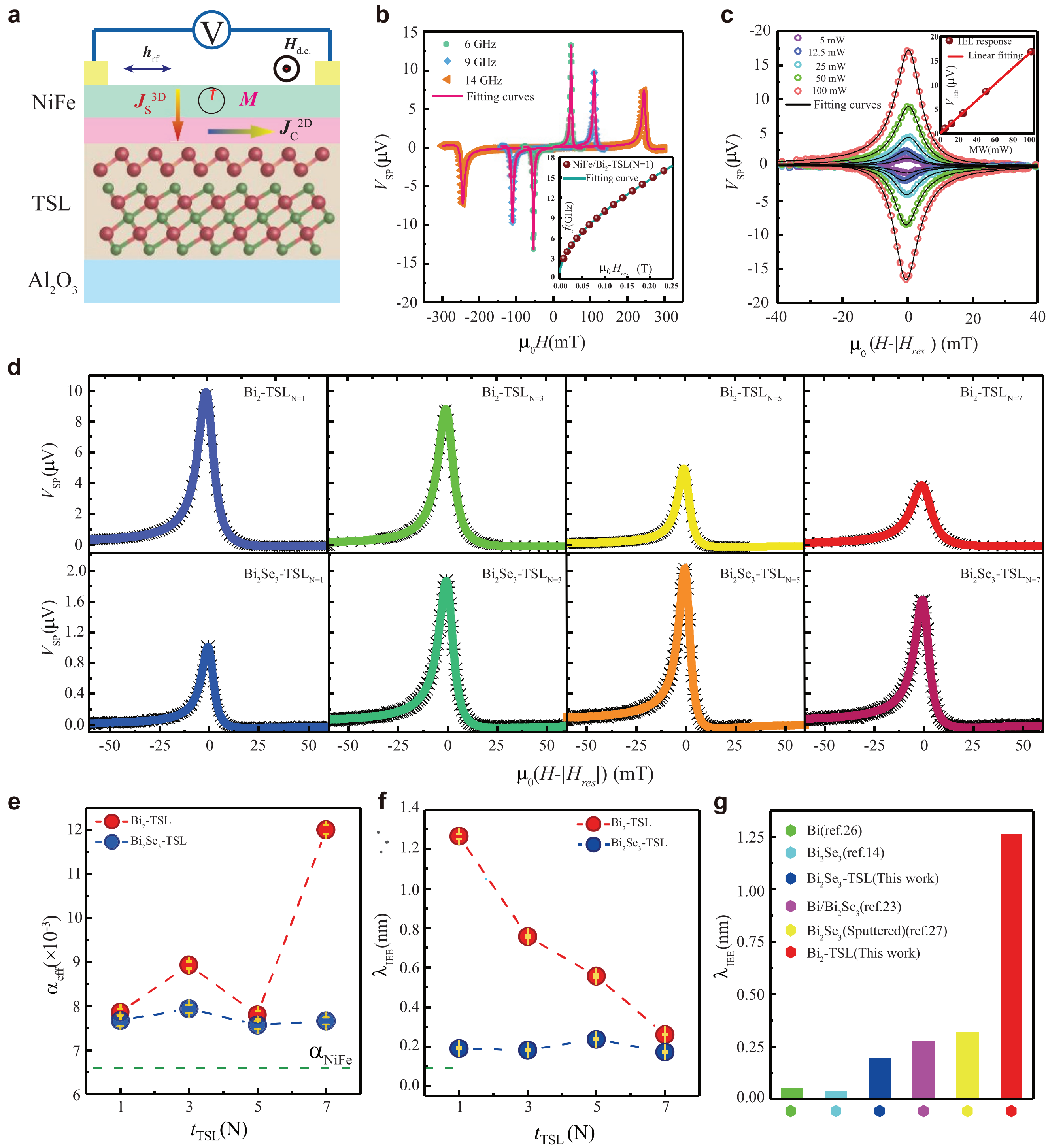

Figure 2. High SCC in the TI superlattices characterized via the spin-pumping approach. a) A sketch of the experimental setup for the spin-pumping experiment in the NiFe/TSL heterostructures. Microwave radiation pumps pure spin currents from the ferromagnetic layer into the adjacent TI superlattice. The injected 3D spin current (J_S^{3D}) gets converted into 2D charge currents (J_C^{2D}) and concomitant charge voltages (V_{SP}) via inverse Edelstein effect due to the surface states in the TI superlattice. b) Field (H) dependence of the spin-pumping-induced voltage $V_{SP}(H)$ in the NiFe/Bi$_2$-TSL$_{N=1}$ heterostructure at different microwave frequencies. The solid lines fits to symmetric and antisymmetric Lorentzian functions with weights of V_{sym} and V_{asy}. The inset shows a plot of frequency versus FMR resonant field (H_{res}) fitted using the Kittel formula, by which the effective magnetization M_{eff} can be derived (see Figure S8b, Supporting Information). c) $V_{SP}(H)$ plot of the NiFe/Bi$_2$-TSL$_{N=3}$ sample under different microwave excitation powers. The inset shows the microwave power dependence of obtained V_{IEE}. The solid line shows the linear fit to the data. d) $V_{SP}(H)$ plot with different stacking periods (N) for the Bi$_2$ termination (top) and Bi$_2$Se$_3$ termination (bottom, respectively). The microwave power is 50 mW and the frequency is fixed at 9 GHz. e,f) Obtained damping factor α and SCC efficiency (λ_{IEE}) as a function of stacking periods N for the TSLs with two terminations. g) A summary of the λ_{IEE} of the Bi-related TIs from the best previous reports and this work(*). All the measurements were taken at 300 K.

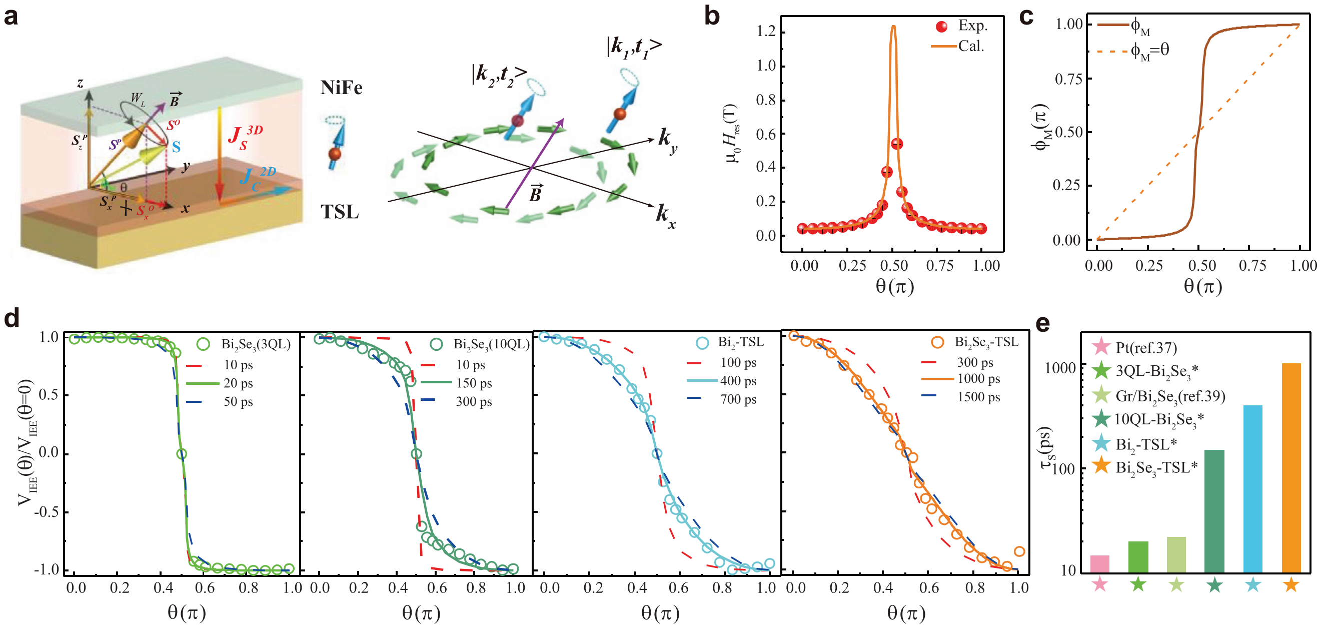

Figure 3. Long spin lifetime (τ_s) in TI superlattices measured by oblique Hanle measurements. a) Schematic geometry of oblique Hanle measurements in the NiFe/TSL heterostructures when the external magnetic field H is applied oblique to the film plane. θ and ϕ_M denotes the magnetic field angle and magnetization angle, respectively. The right panel illustrates the suppressed spin accumulation on the surface state of TSL by the oblique magnetic field that results in a decrease of V_{IEE} response as a function of out-of-plane magnetic field angle θ. b,c) FMR resonant field, $\mu_0 H_{res}$ and magnetization angle ϕ_M as a function of out-of-plane field angle, θ. d) θ dependence IEE response of NiFe/Bi_2Se_3 (3QL), NiFe/Bi_2Se_3 (10QL), NiFe/Bi_2-$TSL_{N=1}$ and NiFe/Bi_2Se_3-$TSL_{N=1}$, respectively. The dashed curves are the theoretical curve with different spin lifetime τ_s. The solid line shows the best simulated curves. e) A summary of the τ_s of the Bi_2Se_3-related spin phenomenon from the previous reports and this work(*).

lifetime up to $\tau_s \approx 1$ ns is observed. It is noteworthy that the TSS-proximity SOC usually reduces τ_s from ns to a few ps in the case of the graphene/TI with high mobility carriers in which the E–Y mechanism and D–P mechanism determines the spin lifetime synergistically.[39,40] According to the obtained inverse relation of τ_p and τ_s between two terminations, the D–P like mechanism would dominate the spin scattering in the presence of coexisting topological nontrivial surface states. From the D–P mechanism,[41] the estimated effective overall SOC strength is about 0.5 meV ($B_{SO} \approx 4.3$ T) for Bi_2-$TSL_{N=1}$ and 0.3 meV ($B_{SO} \approx 2.6$ T) for Bi_2Se_3-$TSL_{N=1}$, respectively, which are roughly the same for both of the two terminations. The similar SOC strength for the two terminations of the TI-superlattice is not surprising as they both arise from the same bulk state of the TI elements as validated by the almost identical band structures at the deeper binding energies below –1.0 eV as measured by ARPES (see Figure S7, Supporting Information).

The change of λ_{IEE} as a function of stacking sequence (N) could be attributed to the evolution of a helical spin-dependent band structure as the stacking period increases, which is the hallmark of the emergent nontrivial TSSs tuned by the quantum confinement effect.[25] **Figure 4** shows the constant energy contour of density at indicated binding energies for the Bi_2Se_3 termination (Figure 4a,b) and Bi_2 termination (Figure 4d,e) states measured by ARPES, respectively. The calculated spin-resolved surface Fermi contour for the two terminations further validates the evolution of band structure modified by stacking sequence as shown in Figure 4c,f, respectively.

For the Bi_2-terminated sample, the calculation in Figure 1g shows a Rashba-like Dirac surface state with nearly linear E–k dispersion extended to higher binding energy.[17,20] The spin vector $\boldsymbol{S}(\boldsymbol{k})$ along the inner and outer circles have opposite spin helicities, revealing the typical signature of the Rashba-like splitting effect. The obtained maximal Fermi vector k_F and Rashba spin momentum splitting Δk_F are 0.9 Å^{-1} with 0.5 Å^{-1} for $N = 1$ and reduces to 0.8 Å^{-1} with 0.46 Å^{-1} at $N = 5$, consistent with the N-dependence of the SCC efficiency. In contrast to the two non-intersecting surface bands extending to the Fermi level in Figure 1d (right), we extracted the $\boldsymbol{S}(\boldsymbol{k})$ at $E_B = -0.4$ eV as the Fermi contour shown solely determined by the Rashba-like Dirac surface state. An approximately 100% in-plane polarization $S_{x,y}$ of the innermost contour was observed while the outmost Fermi contour possesses an opposite spin helicity and relatively large out-of-plane polarization S_z around 33%. However, the overall shape of the Fermi contour is not in good agreement with the Fermi surface topology of TSS enclosed by six pockets shown in Figure 4d,e. It seems that there is a p-type doping about 0.4 eV on the Bi_2-termination due to additional charge transfer from the Bi_2 layer to Bi_2Se_3 layer. The observed anisotropic Fermi surface would arise from complicated high-order terms induced by the emerging U(1) rotational symmetry of the isotropic Dirac cone Hamilton breaking.[42] Also, this may not be easily resolved by the spin-pumping measurement.

For the Bi_2Se_3-terminated TSL with dual TSSs, the outer warped Fermi contour of TSS possesses the same clockwise spin helicity with the TSS of Bi_2Se_3 for their same parity at each TRIM.[43] Meanwhile, the inner warped Fermi contour at the TCI state shows an opposite spin helicity which is inevitably required by two irreducible representations under mirror

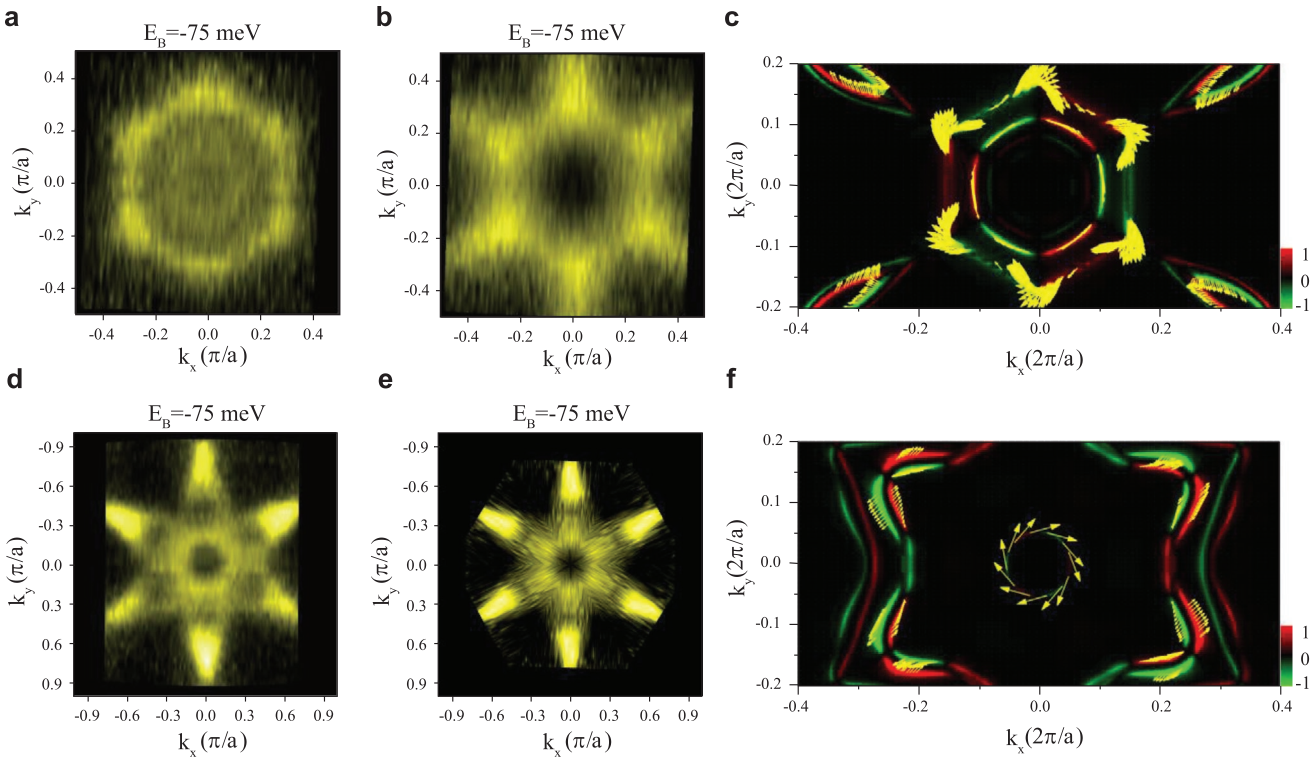

Figure 4. Termination-dependent spin textures in the TI superlattices. a,b) The constant energy contour of density of states measured by ARPES at indicated binding energies for the Bi_2Se_3 termination with $N = 1$ (a) and $N = 5$ (b), respectively, and their corresponding theoretical spin-resolved Fermi contour extracted from the DFT calculations in (c). d,e) The constant energy contour of density of states measured by ARPES at indicated binding energies for the Bi_2 termination with $N = 1$ (d) and $N = 5$ (e, Symmetrized ARPES), respectively, and their corresponding theoretical spin-resolved Fermi contour extracted from the DFT calculations in (f). The yellow arrows indicate the in-plane component of spin vector $S(\mathbf{k})$ while the red and green colors depict its out-of-plane component.

symmetry operation.[22] Nevertheless, the spin momentum locking of coexisting TSSs dually suppress 180° backscattering from non-magnetic impurities, topologically guaranteeing a longer spin lifetime in the dual TI surface. Particularly, the long lifetime of Bi_2Se_3-terminated TSL yields a long spin diffusion length $\lambda_s = \sqrt{D_s \cdot \tau_s}$ whose low boundary ranges up to 430 nm assuming that $D_s = D_c = \sqrt{v_F^2 \cdot \tau_p^*}$ ($\tau_p^* = \tau_p$, τ_p^* represents the original momentum relaxation time inside the TSS).[44]

In conclusion, we found highly efficient spin-to-charge conversion in a topological superlattice, λ_{IEE} up to 1.26 nm with $\Delta\alpha$ just about 1×10^{-3}, together with a comparatively large carrier concentration ≈1.27×10^{15} cm^{-2} according to $n_s = k_F^2/4\pi$. The dual TSS interface phase yields a substantially long spin lifetime of ≈1 ns (the estimated spin diffusion length with lower limit up to 430 nm). Our work heralds the possibility of long-distance interfacial spin transport originating from dual topological symmetry protection. The combination of these novel properties in such a system not only provides new insight into achieving high spin–charge interconversion in topological superlattices but also enables the realization of the family of dual topological superlattices for ultralow energy spin–orbit magnetization switching like future spin–orbit torque devices.[45] The developed dual topological superlattices here may also stimulate future opto-spintronic applications where TIs have been recently explored, such as spin-optoelectronics,[46] spin-galvanic effect,[47] and ultrafast terahertz emission.[48]

Experimental Section

Sample Preparation: The low-dimensional (□/Bi_2Se_3)-(Bi_2/Bi_2Se_3)$_N$ or (Bi_2/Bi_2Se_3)-(Bi_2/Bi_2Se_3)$_N$ (N = 1, 3, 5, or 7) ultrathin films were grown on Si(111) substrate using MBE growth with the base pressure of 5×10^{-10} mbar for ARPES measurements, or on Al_2O_3(0001) substrate followed by deposition of the NiFe top layer (15 nm thick, the composition of NiFe rod is $Ni_{80}Fe_{20}$) via electron beam evaporation without breaking the vacuum for FMR and SP-FMR. The seeding layer 1-QL Bi_2Se_3 was deposited at a lower temperature of 450 K with flux ratio Bi:Se of about 1:15, and then slowly warmed up to 550 K. To form the inserted Bi bilayer, (1 + 2x) BLs Bi were deposited first while Bi and Se were co-deposited upon the formed Bi-bilayer with flux ratio Bi:Se of about 2(1 − x):3 to form Bi_2Se_3 layer. To avoid the fast reaction of Bi bilayer with excess Se to form additional Bi_2Se_3 layers at high temperature, the growth temperature and time were precisely controlled. After several repeated growths of Bi and Bi_2Se_3 layers, the substrate was annealed at 550 K for half an hour and then cooled to room temperature. No significant XRD pattern differences between MBE-grown films and cleaved bulk crystals were observed.

For the microstructure characterization, the reduced-dimensional topological insulator superlattice on Si(111) was prepared by conventional methods, that is, cutting, grinding, dimpling, polishing, and Ar-ion milling with a liquid-nitrogen cooling stage. The annular bright-field scanning transmission electron microscopy (ABF STEM) image in Figure S1a, Supporting Information, shows that TSL on substrate Si(111) has a highly ordered layered structure along the [0001] direction as designed by MBE method (Si(111)//Bi_2Se_3-Bi_2-Bi_2Se_3-Bi_2- ... - ...), with a very sharp interface between the superlattice and Si substrate. The ABF-STEM was fast Fourier transform filtered to the instrumental resolution of about

1 Å. Additionally, the TEM image in Figure S1b, Supporting Information, shows geometry cross-section structure of NiFe/RD-TSL//Al_2O_3 which was prepared by focused ion beam (FIB) milling. The (scanning) transmission electron microscopy (STEM and TEM) studies were conducted using a JEOL ARM-200F atomic resolution analytical electron microscope.

ARPES Measurements: After the growth of $(\square/Bi_2Se_3)\text{-}(Bi_2/Bi_2Se_3)_{N=1,5}$ on Si(111), a 5-nm Se capping layer was deposited on Bi_2Se_3 termination to protect TSS from surface contamination before samples were transferred to another MBE. To probe Bi_2Se_3-terminated band structure, the samples were heated up to 550 K and kept for 1 h to remove Se capper and then transferred to ARPES chamber. After finishing ARPES measurement, the Bi_2Se_3-terminated sample was transferred back to MBE, and 1 BL Bi was deposited at room temperature and annealed at 420 K for 1 h for the ARPES measurement of Bi_2-terminated sample. The ARPES measurements were performed at 10 K with a He discharge lamp with a photon energy of 21.2 eV as the photon source and Scienta DA30 as the electron energy analyzer. The energy and angular resolution were better than 20 meV and 0.5°, respectively.

Spin-Pumping Measurements: FMR was performed at room temperature from 2 to 16 GHz using a commercial NanOsc PhaseFMR spectrometer with a coplanar waveguide, while a GMW electromagnet was used for applying an external magnetic field. For the spin-pumping measurements, microwaves were generated by a Keysight X-Series Microwave Analog Signal Generator at an excitation frequency of 2–16 GHz and microwave power of 50 mW. A transverse dc voltage was electrically detected between two silver paste contacts at opposite ends of the single crystals, recorded by a Stanford Lock-In Amplifier. Oblique Hanle effect measurements were performed by rotating the sample and coplanar waveguide with respect to the applied magnetic field using a precision goniometer, by which both the transverse dc voltage and FMR signal could be recorded simultaneously. All the measurements were taken at room temperature.

DFT Calculation: The electronic structure calculations were performed using density functional theory (Quantum Espresso package) with a plane-wave basis set and ultrasoft pseudopotentials for a $Bi_2\text{-}Bi_2Se_3\text{-}Bi_2\text{-}Bi_2Se_3$ slab.[49] The Perdew–Burke–Ernzerhof formulation was used for the exchange-correlation functional within GGA.[50] The Brillouin zone was sampled with $20 \times 20 \times 1$ equally-spaced momentum points. The ground state energies were converged with respect to the number of k-points, and the wave-function energy cutoff which was set to 40 Rydberg. Spin–orbit coupling was included to account for the spin texture of the surface states. For the slab geometry, $Bi_2Se_3\text{-}Bi_2\text{-}Bi_2Se_3\text{-}Bi_2$ layers consisting of one repeating period with $Bi_2\text{-}Bi_2Se_3$ stacking sequence as shown in Figure 1a with 15 Å of vacuum between adjacent slabs were constructed. For the cell parameters, the experimentally determined lattice parameters and atomic positions were used to construct the slab. The spin projections and the contribution of the atoms from a layer to the overall surface electronic structure were determined by calculating the partial contribution of each atomic basis set in the layer to the wave functions at all k-points.

Supporting Information

Supporting Information is available from the Wiley Online Library or from the author.

Acknowledgements

This work was supported by the National Key Research Program of China (Grant Nos. 2016YFA0300701 and 2017YFB0702702), the National Natural Sciences Foundation of China (Grant Nos. 52031015, 1187411, 51427801, and 51671212), and the Key Research Program of Frontier Sciences, CAS (Grant Nos. QYZDJ-SSW-JSC023, KJZD-SW-M01 and ZDYZ2012-2). S.Y., E.V., and D.S. acknowledges the support from the NC State University–Nagoya Research Collaboration Grant and the NC State Faculty Research and Professional Development (FRPD) program. The calculations were performed at the National Energy Research Scientific Computing Center, a DOE Office of Science User Facility supported by the Office of Science of the U.S. Department of Energy under Contract No. DE-AC02-05CH11231.

Conflict of Interest

The authors declare no conflict of interest.

Author Contributions

R.S., S.Y., and X.Y. contributed equally to this work. D.S. and Z.C. conceived this study and the experiment. R.S. and E.V. fabricated the devices, R.S. and X.Y. performed the ARPES measurements, S.Y. and E.V. measured the FMR, spin pumping, oblique Hanle effect, and calibrated rf field. A.K. and A.F.K were responsible for the DFT calculation. W.X. and B.G. performed STEM measurements. Y.L., N.L., Y. L., and S.Z. helped in sample preparation, ARPES measurement, and electronic structure calculation. W.H. and X.Z. made great contribution to MBE and ARPES setup. D.S. and Z.C. were responsible for the project planning and group managing. R.S., D.S., and Z.C. wrote the paper. All authors discussed the results and worked on data analysis and manuscript preparation.

Keywords

dual topological insulators, spin lifetime, spin-to-charge conversion, spintronics, topological superlattices

Received: August 5, 2020
Revised: September 27, 2020
Published online:

[1] J. Sinova, S. O. Valenzuela, J. Wunderlich, C. H. Back, T. Jungwirth, *Rev. Mod. Phys.* **2015**, *87*, 1213.
[2] V. M. Edelstein, *Solid State Commun.* **1990**, *73*, 233.
[3] M. Z. Hasan, C. L. Kane, *Rev. Mod. Phys.* **2010**, *82*, 3045.
[4] A. Dankert, J. Geurs, M. V. Kamalakar, S. Charpentier, S. P. Dash, *Nano Lett.* **2015**, *15*, 7976.
[5] J. C. Rojas-Sanchez, S. Oyarzun, Y. Fu, A. Marty, C. Vergnaud, S. Gambarelli, L. Vila, M. Jamet, Y. Ohtsubo, A. Taleb-Ibrahimi, P. Le Fevre, F. Bertran, N. Reyren, J. M. George, A. Fert, *Phys. Rev. Lett.* **2016**, *116*, 096602.
[6] A. Dankert, P. Bhaskar, D. Khokhriakov, I. H. Rodrigues, B. Karpiak, M. V. Kamalakar, S. Charpentier, I. Garate, S. P. Dash, *Phys. Rev. B* **2018**, *97*, 125414.
[7] Z. K. Liu, J. Jiang, B. Zhou, Z. J. Wang, Y. Zhang, H. M. Weng, D. Prabhakaran, S. K. Mo, H. Peng, P. Dudin, T. Kim, M. Hoesch, Z. Fang, X. Dai, Z. X. Shen, D. L. Feng, Z. Hussain, Y. L. Chen, *Nat. Mater.* **2014**, *13*, 677.
[8] D. MacNeill, G. M. Stiehl, M. H. D. Guimaraes, R. A. Buhrman, J. Park, D. C. Ralph, *Nat. Phys.* **2017**, *13*, 300.
[9] A. A. Burkov, *Annu. Rev. Condens. Matter Phys.* **2018**, *9*, 359.
[10] B. Zhao, B. Karpiak, D. Khokhriakov, A. Johansson, A. M. Hoque, X. Xu, Y. Jiang, I. Mertig, S. P. Dash, *Adv. Mater.* **2020**, *32*, 2000818.
[11] B. Zhao, D. Khokhriakov, Y. Zhang, H. Fu, B. Karpiak, A. M. Hoque, X. Xu, Y. Jiang, B. Yan, S. P. Dash, *Phys. Rev. Res.* **2020**, *2*, 013286.

[12] A. R. Mellnik, J. S. Lee, A. Richardella, J. L. Grab, P. J. Mintun, M. H. Fischer, A. Vaezi, A. Manchon, E. A. Kim, N. Samarth, D. C. Ralph, *Nature* **2014**, *511*, 449.
[13] Y. Fan, X. Kou, P. Upadhyaya, Q. Shao, L. Pan, M. Lang, X. Che, J. Tang, M. Montazeri, K. Murata, L.-T. Chang, M. Akyol, G. Yu, T. Nie, K. L. Wong, J. Liu, Y. Wang, Y. Tserkovnyak, K. L. Wang, *Nat. Nanotechnol.* **2016**, *11*, 352.
[14] H. Wang, J. Kally, J. S. Lee, T. Liu, H. Chang, D. R. Hickey, K. A. Mkhoyan, M. Wu, A. Richardella, N. Samarth, *Phys. Rev. Lett.* **2016**, *117*, 076601.
[15] J. B. S. Mendes, O. Alves Santos, J. Holanda, R. P. Loreto, C. I. L. de Araujo, C.-Z. Chang, J. S. Moodera, A. Azevedo, S. M. Rezende, *Phys. Rev. B* **2017**, *96*, 180415(R).
[16] M. Eschbach, M. Lanius, C. Niu, E. Młyńczak, P. Gospodarič, J. Kellner, P. Schüffelgen, M. Gehlmann, S. Döring, E. Neumann, M. Luysberg, G. Mussler, L. Plucinski, M. Morgenstern, D. Grützmacher, G. Bihlmayer, S. Blügel, C. M. Schneider, *Nat. Commun.* **2017**, *8*, 14976.
[17] T. Valla, H. Ji, L. M. Schoop, A. P. Weber, Z. H. Pan, J. T. Sadowski, E. Vescovo, A. V. Fedorov, A. N. Caruso, Q. D. Gibson, L. Müchler, C. Felser, R. J. Cava, *Phys. Rev. B* **2012**, *86*, 241101(R).
[18] L. Fleet, *Nat. Phys.* **2017**, *13*, 8.
[19] H. Okamoto, *J. Phase Equilib.* **1994**, *15*, 195.
[20] Q. D. Gibson, L. M. Schoop, A. P. Weber, H. Ji, S. Nadj-Perge, I. K. Drozdov, H. Beidenkopf, J. T. Sadowski, A. Fedorov, A. Yazdani, T. Valla, R. J. Cava, *Phys. Rev. B* **2013**, *88*, 081108(R).
[21] J. Zhang, X. Liu, G. Huang, *Phys. Status Solidi B* **2015**, *252*, 2090.
[22] A. P. Weber, Q. D. Gibson, H. Ji, A. N. Caruso, A. V. Fedorov, R. J. Cava, T. Valla, *Phys. Rev. Lett.* **2015**, *114*, 256401.
[23] R. Sun, S. Yang, X. Yang, E. Vetter, D. Sun, N. Li, L. Su, Y. Li, Y. Li, Z. Z. Gong, Z. K. Xie, K. Y. Hou, Q. Gul, W. He, X. Q. Zhang, Z. H. Cheng, *Nano Lett.* **2019**, *19*, 4420.
[24] V. Sunko, H. Rosner, P. Kushwaha, S. Khim, F. Mazzola, L. Bawden, O. J. Clark, J. M. Riley, D. Kasinathan, M. W. Haverkort, T. K. Kim, M. Hoesch, J. Fujii, I. Vobornik, A. P. Mackenzie, P. D. C. King, *Nature* **2017**, *549*, 492.
[25] M. S. Bahramy, P. D. King, A. de la Torre, J. Chang, M. Shi, L. Patthey, G. Balakrishnan, P. Hofmann, R. Arita, N. Nagaosa, F. Baumberger, *Nat. Commun.* **2012**, *3*, 1159.
[26] C. Zucchetti, M. T. Dau, F. Bottegoni, C. Vergnaud, T. Guillet, A. Marty, C. Beigne, S. Gambarelli, A. Picone, A. Calloni, G. Bussetti, A. Brambilla, L. Duo, F. Ciccacci, P. K. Das, J. Fujii, I. Vobornik, M. Finazzi, M. Jamet, *Phys. Rev. B* **2018**, *98*, 184418.
[27] M. Dc, J. Y. Chen, T. Peterson, P. Sahu, B. Ma, N. Mousavi, R. Harjani, J. P. Wang, *Nano Lett.* **2019**, *19*, 4836.
[28] J. C. R. Sánchez, L. Vila, G. Desfonds, S. Gambarelli, J. P. Attané, J. M. De Teresa, C. Magén, A. Fert, *Nat. Commun.* **2013**, *4*, 2944.
[29] M. Hajlaoui, E. Papalazarou, J. Mauchain, L. Perfetti, A. Taleb-Ibrahimi, F. Navarin, M. Monteverde, P. Auban-Senzier, C. R. Pasquier, N. Moisan, D. Boschetto, M. Neupane, M. Z. Hasan, T. Durakiewicz, Z. Jiang, Y. Xu, I. Miotkowski, Y. P. Chen, S. Jia, H. W. Ji, R. J. Cava, M. Marsi, *Nat. Commun.* **2014**, *5*, 3003.
[30] R. Dey, N. Prasad, L. F. Register, S. K. Banerjee, *Phys. Rev. B* **2018**, *97*, 174406.
[31] M. Popinciuc, C. Józsa, P. J. Zomer, N. Tombros, A. Veligura, H. T. Jonkman, B. J. van Wees, *Phys. Rev. B* **2009**, *80*, 214427.
[32] W. Han, R. K. Kawakami, M. Gmitra, J. Fabian, *Nat. Nanotechnol.* **2014**, *9*, 794.
[33] K. Ando, E. Saitoh, *Nat. Commun.* **2012**, *3*, 629.
[34] S.-J. Wang, D. Venkateshvaran, M. R. Mahani, U. Chopra, E. R. McNellis, R. Di Pietro, S. Schott, A. Wittmann, G. Schweicher, M. Cubukcu, K. Kang, R. Carey, T. J. Wagner, J. N. M. Siebrecht, D. P. G. H. Wong, I. E. Jacobs, R. O. Aboljadayel, A. Ionescu, S. A. Egorov, S. Mueller, O. Zadvorna, P. Skalski, C. Jellett, M. Little, A. Marks, I. McCulloch, J. Wunderlich, J. Sinova, H. Sirringhaus, *Nat. Electron.* **2019**, *2*, 98.
[35] S. Yang, E. Vetter, T. Wang, A. Amassian, D. Sun, *J. Phys.: Mater.* **2020**, *3*, 015012.
[36] D. C. Vaz, P. Noel, A. Johansson, B. Gobel, F. Y. Bruno, G. Singh, S. McKeown-Walker, F. Trier, L. M. Vicente-Arche, A. Sander, S. Valencia, P. Bruneel, M. Vivek, M. Gabay, N. Bergeal, F. Baumberger, H. Okuno, A. Barthelemy, A. Fert, L. Vila, I. Mertig, J. P. Attane, M. Bibes, *Nat. Mater.* **2019**, *18*, 1187.
[37] C. Fang, C. H. Wan, B. S. Yang, J. Y. Qin, B. S. Tao, H. Wu, X. Zhang, X. F. Han, A. Hoffmann, X. M. Liu, Z. M. Jin, *Phys. Rev. B* **2017**, *96*, 134421.
[38] J. Xu, T. Zhu, Y. K. Luo, Y. M. Lu, R. K. Kawakami, *Phys. Rev. Lett.* **2018**, *121*, 127703.
[39] D. Khokhriakov, A. W. Cummings, K. Song, M. Vila, B. Karpiak, A. Dankert, S. Roche, S. P. Dash, *Sci. Adv.* **2018**, *4*, eaat9349.
[40] D. Khokhriakov, A. M. Hoque, B. Karpiak, S. P. Dash, *Nat. Commun.* **2020**, *11*, 3657.
[41] B. Yang, M.-F. Tu, J. Kim, Y. Wu, H. Wang, J. Alicea, R. Wu, M. Bockrath, J. Shi, *2D Mater.* **2016**, *3*, 031012.
[42] L. Fu, *Phys. Rev. Lett.* **2009**, *103*, 266801.
[43] Z. H. Pan, E. Vescovo, A. V. Fedorov, D. Gardner, Y. S. Lee, S. Chu, G. D. Gu, T. Valla, *Phys. Rev. Lett.* **2011**, *106*, 257004.
[44] D. Culcer, *Phys. E* **2012**, *44*, 860.
[45] K. Cai, Z. Zhu, J. M. Lee, R. Mishra, L. Ren, S. D. Pollard, P. He, G. Liang, K. L. Teo, H. Yang, *Nat. Electron.* **2020**, *3*, 37.
[46] Y. Pan, Q. Z. Wang, A. L. Yeats, T. Pillsbury, T. C. Flanagan, A. Richardella, H. Zhang, D. D. Awschalom, C. X. Liu, N. Samarth, *Nat. Commun.* **2017**, *8*, 1037.
[47] J. Yu, X. Zeng, L. Zhang, K. He, S. Cheng, Y. Lai, W. Huang, Y. Chen, C. Yin, Q. Xue, *Nano Lett.* **2017**, *17*, 7878.
[48] X. Wang, L. Cheng, D. Zhu, Y. Wu, M. Chen, Y. Wang, D. Zhao, C. B. Boothroyd, Y. M. Lam, J. X. Zhu, M. Battiato, J. C. W. Song, H. Yang, E. E. M. Chia, *Adv. Mater.* **2018**, *30*, 1802356.
[49] P. Giannozzi, S. Baroni, N. Bonini, M. Calandra, R. Car, C. Cavazzoni, D. Ceresoli, G. L. Chiarotti, M. Cococcioni, I. Dabo, A. Dal Corso, S. de Gironcoli, S. Fabris, G. Fratesi, R. Gebauer, U. Gerstmann, C. Gougoussis, A. Kokalj, M. Lazzeri, L. Martin-Samos, N. Marzari, F. Mauri, R. Mazzarello, S. Paolini, A. Pasquarello, L. Paulatto, C. Sbraccia, S. Scandolo, G. Sclauzero, A. P. Seitsonen, A. Smogunov, P. Umari, R. M. Wentzcovitch, *J. Phys.: Condens. Matter* **2009**, *21*, 395502.
[50] J. P. Perdew, K. Burke, M. Ernzerhof, *Phys. Rev. Lett.* **1996**, *77*, 3865.